ACS APPLIED MATERIALS & INTERFACES

Research Article

www.acsami.org

Improving the Magnetic Properties of Co–CoO Systems by Designed Oxygen Implantation Profiles

Enric Menéndez,*[,†,‡] Joost Demeter,[†] Jelle Van Eyken,[†] Przemyslaw Nawrocki,[§] Ewa Jedryka,[§] Marek Wójcik,[§] José Francisco Lopez-Barbera,[‡] Josep Nogués,*[,‡,⊥] André Vantomme,[†] and Kristiaan Temst*[,†]

[†]Instituut voor Kern- en Stralingsfysica, KU Leuven, Celestijnenlaan 200 D, B-3001 Leuven, Belgium

[‡] Catalan Institute of Nanotechnology, CIN2(ICN-CSIC), Universitat Autònoma de Barcelona, Campus de la UAB, Bellaterra, 08193 Barcelona, Spain

[§]Institute of Physics, Polish Academy of Sciences, Al. Lotnikow 32/46, Warszawa 02-668, Poland

[⊥]Institució Catalana de Recerca i Estudis Avançats (ICREA), Barcelona, Spain

Supporting Information

ABSTRACT: Oxygen implantation in ferromagnetic Co thin films is shown to be an advantageous route to improving the magnetic properties of Co–CoO systems by forming multiple nanoscaled ferromagnetic/antiferromagnetic interfaces homogeneously distributed throughout the layer. By properly designing the implantation conditions (energy and fluence) and the structure of the films (capping, buffer, and Co layer thickness), relatively uniform O profiles across the Co layer can be achieved using a single-energy ion implantation approach. This optimized configuration results in enhanced exchange bias loop shifts, improved loop homogeneity, increased blocking temperature, reduced relative training effects and increased retained remanence in the trained state with respect to both Co/CoO bilayers and O-implanted Co films with a Gaussian-like O depth profile. This underlines the great potential of ion implantation to tailor the magnetic properties by controllably modifying the local microstructure through tailored implantation profiles.

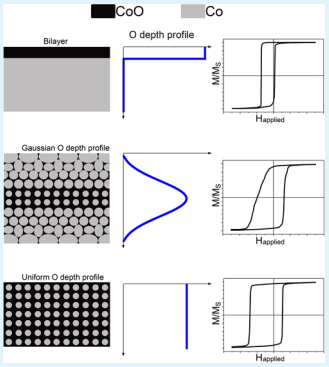

KEYWORDS: *thin films, capping layer, ion implantation, magnetic properties, exchange bias, structure-property relationships*

INTRODUCTION

Ion irradiation has been extensively used to manipulate the magnetic properties of materials,[1−3] including exchange bias (EB).[4−6] In contrast, the use of nonmagnetic ion implantation (e.g., H, O or N) to control the magnetic properties of materials is scarcer.[7−9] EB refers to the interface exchange coupling between a ferromagnetic (FM) and an antiferromagnetic (AFM) material which leads to a range of interesting effects. The most prominent properties of EB FM/AFM systems is the presence of a shift of the hysteresis loop along the field axis accompanied by a coercivity enhancement.[10,11] In the last decades, EB has gained technological importance since it is used to establish a reference direction in spintronic devices, such as magnetic heads of hard disk drives.[12,13] The vast majority of EB research has been primarily focused on thin film systems, in which Co and CoO are the archetypal FM and AFM materials, respectively. This is mainly due to the essential role of exchange-biased thin films in spintronics.[11] Conventionally, the formation of AFM CoO in Co thin films relies on surface oxidation by exposing the sample to air or to a controlled oxygen atmosphere. Since surface oxidation is a self-limiting process, it results in an oxide thickness of only a few nanometers, forming a bilayer with a single interface between Co and CoO.[14] Interestingly, ion implantation has recently been demonstrated as a suitable alternative approach to form AFM oxides embedded in a FM matrix. Specifically, it has been shown that implantation of O ions into thin FM Co and Ni films locally induces the formation of AFM Co and Ni oxides, respectively, giving rise to EB and, therefore, showing an innovative functional application for ion implantation.[7,15] In contrast to Co/CoO bilayers, ion implantation results in multiple FM/AFM interfaces (i.e. granular-like) distributed throughout the layer.[16] This configuration does not only lead to an enhanced EB shift for a given thickness of the FM layer[15,16] but also to significant changes in properties, such as the magnetic reversal mechanism.[7] However, the use of O-ion implantation to form Co–CoO structures has an inherent drawback. Namely, the Gaussian-like profiles associated with conventional ion implantation lead to an inhomogeneous oxygen profile in the films (Figure 1). This, in turn, brings about a broad distribution of Co–CoO couplings along the depth of the Co layer, resulting in rather heterogeneous magnetic properties revealed by atypical hysteresis loops (Figure 1b).[7,15,16] Such highly asymmetric loops may be

Received: February 7, 2013
Accepted: April 15, 2013
Published: April 15, 2013

   dx.doi.org/10.1021/am400529r | ACS Appl. Mater. Interfaces 2013, 5, 4320−4327

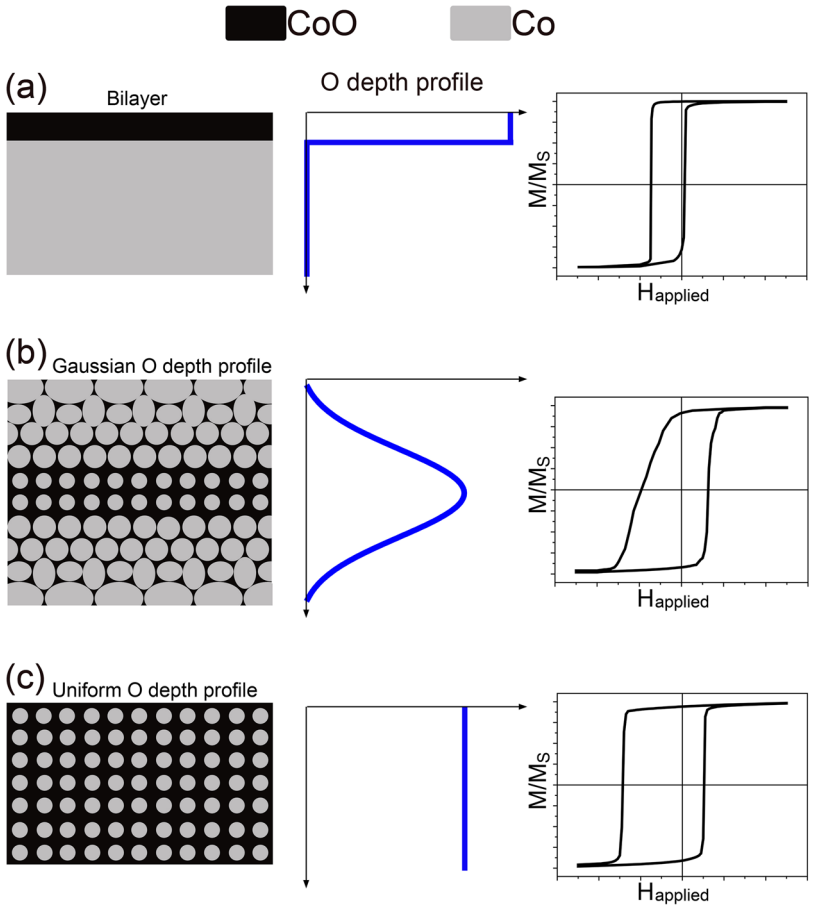

Figure 1. Schematic representation of the microstructure (left colum), the oxygen depth profile (middle column) and hysteresis loops (right column) for (a) Co/CoO bilayers, (b) O-implanted samples with Gaussian-like O depth profiles, and (c) O-implanted samples with a uniform O depth distribution.

detrimental for certain applications, such as magnetic recording media or spintronics where, for instance, well-defined reference directions are required.

In this article, we present an innovative single-energy ion implantation approach in which, by tailoring the implantation parameters and the characteristics and thicknesses of the layers, a rather homogeneous implanted O profile is obtained. The uniform O profile leads to improved exchange bias properties with respect to both Co/CoO bilayers and Gaussian-like O profile implantation. In particular, for optimal conditions, both the loop shift and the blocking temperature are enhanced with respect to previous approaches. Moreover, other aspects, such as training effects, can also be conveniently tuned by the implantation conditions.

EB originates from the interfacial interaction between a FM and an AFM material. After cooling the sample in a magnetic field below the Néel temperature (T_N) of the AFM, a shift (H_E), which is commonly used to determine the strength of EB, and a broadening of the hysteresis loop of the FM (coercivity, H_C, enhancement) are typically observed.[10,11,17] The temperature at which H_E vanishes is denoted as the blocking temperature (T_B). Commonly, due to finite-size effects (i.e., deviations from bulk properties as dimensions are reduced), T_B can be lower than T_N.[10,11,17−20] Another interesting property of EB systems is the so called training effect, i.e., the monotonic decrease in H_E when cycling the system through consecutive hysteresis loops down to a steady value, $H_E^{n=\infty}$ (n labels the number of measured hysteresis loops).[10,11,17,21,22]

RESULTS AND DISCUSSION

As can be seen in Figure 2, TRIM (transport of ions in matter)[23,24] simulations evidence that diverse combinations of capping and buffer layer thicknesses, Co layer thickness and ion implantation energies and fluences can give rise to very different O profiles across the Co layer. In most cases, the O profile is highly inhomogeneous (e.g., Gaussian-like; see Figure 2a, b), which leads to an undesired spread of the magnetic properties.[7,15,16] In fact, because of the stochastic nature of ion−solid interactions, any implanted species into a target material shows a Gaussian-like depth distribution of implanted atoms which brings associated a certain variance around its maximum (see Figure S1 in the Supporting Information).[25] However, by increasing the thickness of the Au capping layer, decreasing that of the Co layer and introducing a Au buffer layer, relatively homogeneous O profiles across the Co layer are obtained, despite a slight increase of O with depth (Figure 2c, d). Even though the use of a capping layer is strictly indispensable to protect the Co from surface oxidation (see Experimental Section), its thickness plays a significant role in order to locate the maximum of the O depth distribution in the Co layer, leaving the low O tail of the distribution in the capping layer (see Figure S1 in the Supporting Information). Moreover, the use of a buffer layer not only acts as a barrier for the O ions but it also avoids atomic intermixing between Co and SiO_2 upon implantation by O backscattering (see Figure S2 in the Supporting Information), which would eventually yield

dx.doi.org/10.1021/am400529r | ACS Appl. Mater. Interfaces 2013, 5, 4320−4327

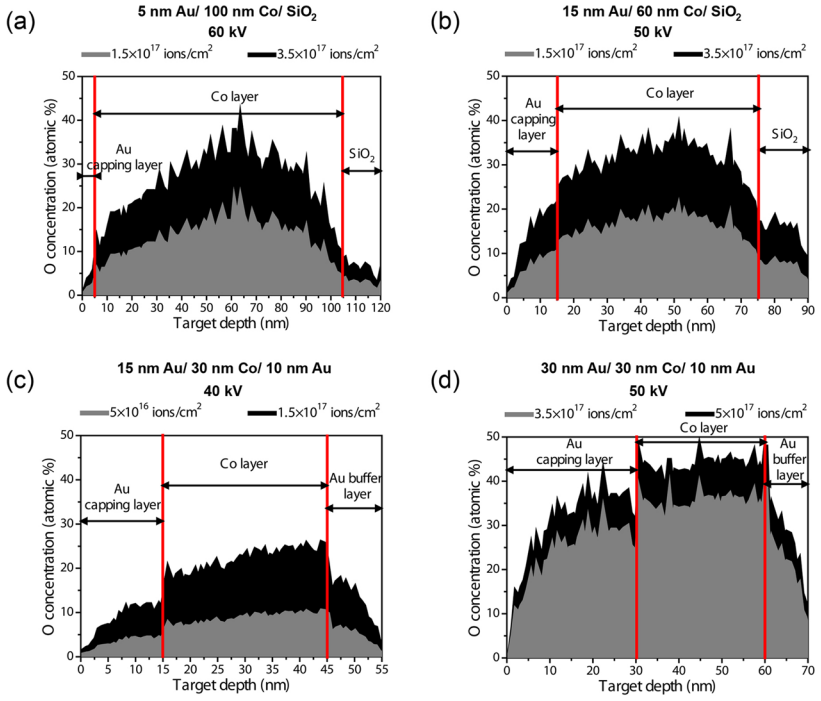

Figure 2. TRIM simulations of the distribution of O atoms (i.e., O depth profile) for different implantation conditions and sample designs consisting of a capping layer/Co layer/buffer layer/substrate: (a) 60 keV O ions into 5 nm Au, 100 nm Co and SiO_2 (substrate) for 1.5×10^{17} and 3.5×10^{17} ions/cm^2; (b) 50 keV O ions into 15 nm Au, 60 nm Co and SiO_2 (substrate) for 1.5×10^{17} and 3.5×10^{17} ions/cm^2; (c) 40 keV O ions into 15 nm Au, 30 nm Co, and 10 nm Au (buffer) for 5×10^{16} and 1.5×10^{17} ions/cm^2; and (d) 50 keV O ions into 30 nm Au, 30 nm Co, and 10 nm Au (buffer) for 3.5×10^{17} and 5×10^{17} ions/cm^2. The fluences in panels a and b were chosen in order to compare the O depth profile when the O content is rather low and high, respectively.

unintended (i.e., not coming from implantation) and uncontrolled incorporation of O in Co. In fact, according to the TRIM simulations, the extent of Co intermixing in SiO_2 can be several nm depending on the conditions. For example, the intermixed SiO_2/Co zone in a Au (15 nm)/Co (30 nm)/SiO_2 (10 nm) sample implanted with 40 keV O ions is more than 3 nm.

Concerning the structural characterization, the NMR spectra at 4.2 K (Figure 3a), taken after cooling in zero applied magnetic field from room temperature, demonstrate that the as-deposited film consists of a mixture of face-centered cubic (FCC) Co and hexagonal close-packed (HCP) Co environments and stacking faults. The NMR line at 217 MHz corresponds to FCC-Co and the lines between 220 and 228 MHz correspond to HCP-Co. The signal between the FCC and HCP-Co lines indicates the existence of stacking faults, which are stacking alterations of the atomic planes, in both Co phases. The low frequency tail in the NMR spectra originates from defects, such as grain boundaries,[26,27] and the interfaces with the Au buffer and the capping layer. Upon oxygen implantation, the amount of crystalline metallic Co significantly decreases because of the increased density of defects within the Co layer and due to the CoO formation. Although the antiferromagnetic CoO phase is not directly observed in the present experiment (it would give a ^{59}Co NMR line in the 500 MHz region and require a much stronger radio frequency field), its presence can be inferred from the increase of the average restoring field after O implantation (Figure 3b). The presence of AFM CoO exchange-coupled to FM Co will obviously modify the restoring field acting on the ferromagnetic part of the sample, depending on the concentration of CoO and its spatial distribution. Whereas the experiment shows that the restoring field increases with oxygen content, the growing ratio tends to some extent to slow down, suggesting a trend towards saturation for the restoring field of high O content samples. Another effect readily visible in the NMR spectra (Figure 3a) is the pronounced enlargement of the low frequency part of the spectrum, observed already at the smallest oxygen fluence, reflecting a strong modification of the grain boundary/interface region. Nonetheless, while the stacking fault density increases in detriment of crystalline Co with increased fluence, the low-frequency tail remains rather unaltered (this part of the spectra overlaps in the implanted samples). This may indicate that implantation results in a grain boundary density which is to some extent fluence independent which is in concordance with the reported grain boundary oxidation mechanism for these O-implanted systems.[16] Thus, beyond a certain fluence, the main role of the implanted oxygen would be to further oxidize the grain boundaries, leading to the growth of the CoO counterpart.

The room-temperature magnetic characterization of the samples shows that, whereas H_C increases monotonically with implantation fluence (from $\mu_0 H_C \approx 6$ mT for unimplanted samples to $\mu_0 H_C \approx 11$ mT for high fluences), the remanence, M_R, normalized to the saturation magnetization, M_S, M_R/M_S decreases slightly. For example, while the film implanted at 3×10^{16} ions/cm^2 shows a M_R/M_S value of around 92%, the sample implanted at 3.5×10^{17} ions/cm^2 exhibits a value of approximately 88%. Moreover, angular-dependent measurements (not shown) indicate that the magnetic properties are isotropic in-plane. Thus, the room temperature magnetic properties are in line with the structural characterization: the as-obtained film is polycrystalline with a random in-plane orientation. The increase in coercivity with ion implantation is

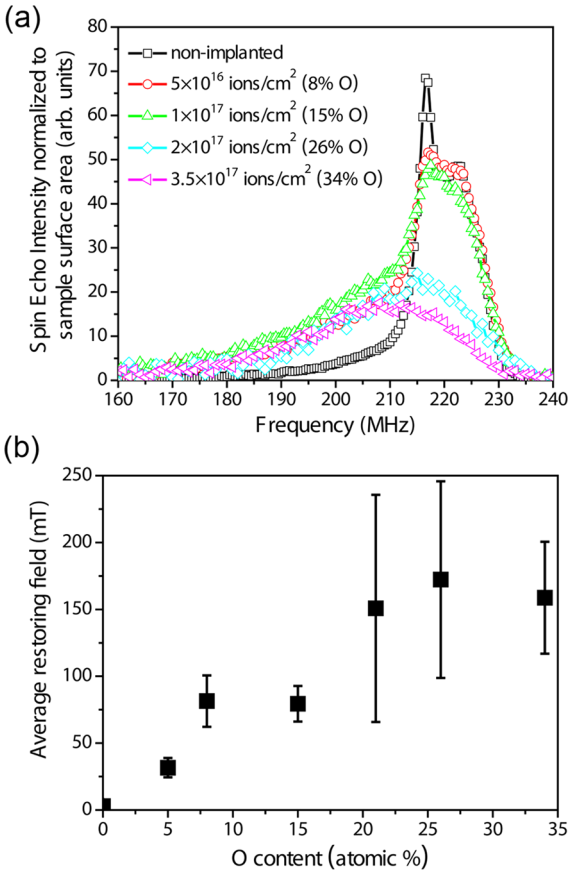

Figure 3. (a) ^{59}Co nuclear magnetic resonance (NMR) spectra, taken at 4.2 K, corresponding to the nonimplanted sample and samples implanted with O ions at 5×10^{16}, 1×10^{17}, 2×10^{17}, and 3.5×10^{17} ions/cm^2. (b) Dependence of the average restoring field on the implanted fluence at 4.2 K. The lines in (a) are connections between the data. The worsening with fluence of the signal to noise ratio (i.e., increase in the error bars) is mainly ascribed to the decrease of metallic Co with fluence and to the small size of the assessed samples. Note that the spectra of the samples implanted at 2×10^{17} and 3.5×10^{17} ions/cm^2 have been smoothened.

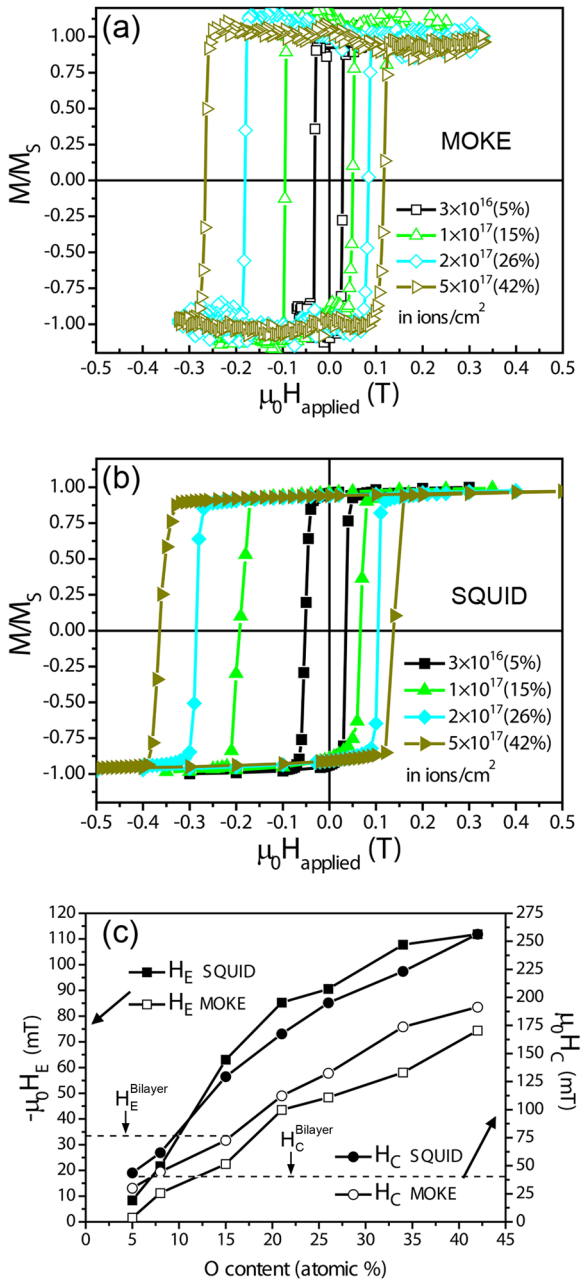

Figure 4. (a) Longitudinal MOKE and (b) SQUID measurements corresponding to the samples implanted at 3×10^{16} (5% O), 1×10^{17} (15% O), 2×10^{17} (26% O), and 5×10^{17} ions/cm^2 (42% O), performed at 10 K. (c) Dependence of the exchange bias shift, H_E, and the coercivity, H_C, on the oxygen content. H_E and H_C for the bilayer sample are highlighted by dashed lines. The lines are connections between points.

essentially ascribed to the increase in the number of defects (such as stacking faults), as confirmed by NMR, that can act as pinning centers for magnetization reversal and, therefore, result in an enhanced coercivity. Upon irradiation, increasing amounts of oxygen accumulate at the grain boundaries forming CoO, decreasing both the exchange and dipolar interactions between grains and reducing the grain size, which should also increase H_C of the Co layers.[28] Moreover, the exchange interactions between the Co grains and the CoO at the grain boundaries could also contribute to the observed increase of H_C with fluence.[29] Even though the remanence decreases slightly with fluence, the longitudinal MOKE hysteresis loops at room temperature (not shown) are rather square-shaped (M_R/M_S values ≥88% for all the samples). Because polycrystalline materials usually exhibit a lower remanence than highly ordered crystalline structures,[28] this reduction implies that implantation leads to a higher degree of structural disorder, in agreement with the NMR characterization and previously reported results.[16]

Figure 4a shows the 10 K longitudinal MOKE hysteresis loops of the different samples after field cooling. The first remarkable feature of the loops is that they are rather symmetric in shape, in contrast to O-implanted samples with Gaussian-like O depth profiles which display rather inhomogeneous loops (i.e., loops with broad distributions of bias fields, see Figure 1b).[7,15,16] Moreover, the longitudinal MOKE loops are characterized by sharp descending and ascending branches (i.e., magnetization inversion takes place at relatively well-defined switching fields), confirming the homogeneity of the O profile. Nonetheless, although the shape of the loops of the implanted samples is also more symmetric than the conventional surface oxidized Co films (which typically show a square branch for a decreasing field and a rounded branch when

dx.doi.org/10.1021/am400529r | ACS Appl. Mater. Interfaces 2013, 5, 4320−4327

increasing the field, see Figure 1a), traces of the aforementioned shape asymmetry between the reversal of the decreasing and the increasing branches cannot be ruled out (i.e., the ascending branch is slightly more rounded than the descending one, see Figures 4a, 4b, and 6b).

In contrast to the MOKE hysteresis loops (Figure 4a), which are characterized by sharp descending and ascending branches with almost full remanence, the SQUID loops (Figure 4b) show slightly lower remanences and a more gradual reversal. Nevertheless, magnetization inversion still takes place at relatively well-defined switching fields. Moreover, the exchange bias shifts, H_E, obtained by SQUID are somewhat larger than by MOKE (Figure 4). Because MOKE penetrates only partially ($\approx$ 10 nm) into the Co layer, the results imply that H_E close to the surface is smaller than H_E at the bottom. In analogy with compositionally graded materials,[30] the difference in H_E can be linked to a O-gradient in our samples (although a simple inhomogeneous reversal independent of the O-gradient cannot be ruled out). Given the dependence of H_E on the AFM thickness,[31] it can be inferred that the O concentration slightly increases (leading to thicker CoO grain boundaries) with depth, in agreement with the simulations in panels c and d in Figure 2.

As can be seen in Figure 4c, both H_E and H_C increase with fluence and, hence, with O concentration. Notably, an increase in H_C can be taken as positive in applications where large H_C is required (e.g., permanent magnets[32] or stabilizing magnetic bits[33]), although it could also be detrimental for certain applications where low H_C would be desirable (e.g., reference layers in certain devices[12]). Concerning H_E, its rate of increase with implantation fluence tends to decrease for high ion fluences, in agreement with previously reported results.[14] This increase in H_C and H_E can be understood as arising from both the larger number of FM/AFM interfaces[34,35] and the increase of the amount of structural defects, such as stacking faults, in Co with increasing O fluence.[36] Remarkably, H_E for high fluences is rather large, reaching values in excess of $\mu_0 H_E = -110$ mT for O fluences of 5×10^{17} ions/cm^2 (42% O). These values are considerably larger than those of Co/CoO bilayers of the same total thickness grown under the same conditions, which only reach $\mu_0 H_E = -33$ mT (Figure 4c). In fact, H_E for the homogeneously implanted films is also larger than for layers implanted with a Gaussian-like O profile.[7,15,16] Other aspects may also play a role in the increase of H_E with fluence, specially after implanting at fluences larger than 5×10^{16} ions/cm^2, from which the grain boundary density remains rather constant. Namely, the increase in magnetocrystalline anisotropy of the formed CoO with large fluences is because of its enlargement and probably its evolution to a more stoichiometric (i.e., less defective) AFM compound which should lead to a larger H_E.[31,37] Furthermore, in the framework of the domain state model,[38] ion implantation may lead to an AFM (i.e., CoO) with increased volume domains which are known to enhance the exchange bias shift.[39] Finally, the increase in CoO with fluence must arise from a reduction of the size of the Co regions. Given that H_E is inversely proportional to the size of the FM constituent,[10,11,17] any decrease in the Co size should bring about an enhancement of H_E.

Another significant feature of the homogeneously implanted films is their blocking temperature. As can be seen in Figure 5, T_B increases monotonically as the O fluence increases, reaching beyond $T_B = 200$ K for large fluences. This is once more in line with the structural characterization since at larger fluences the

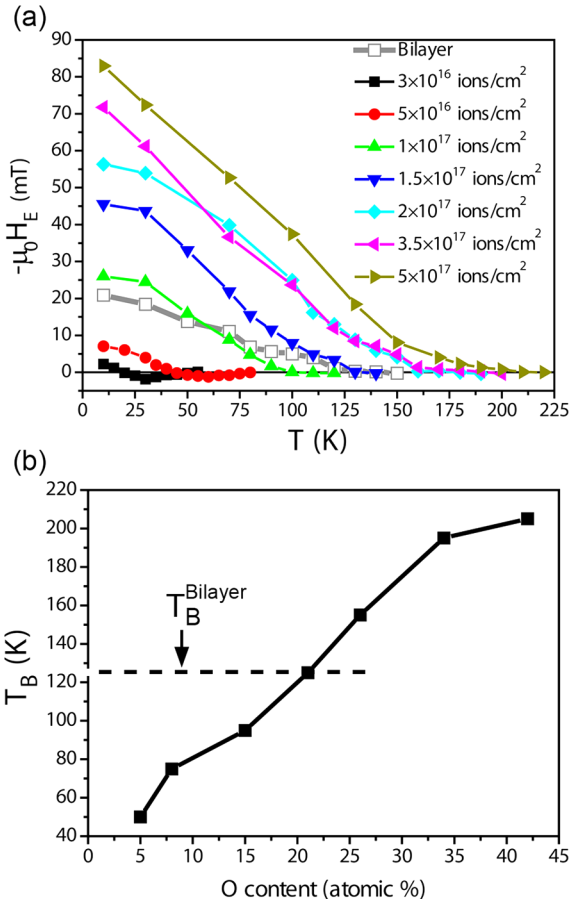

Figure 5. (a) Temperature dependence of the exchange bias shift, H_E, for the bilayer and for the different implanted samples. (b) Dependence of the blocking temperature on the oxygen content. The lines are connections between the data. T_B for the bilayer is highlighted by a dashed line.

CoO grain boundaries become thicker and probably more stoichiometric (with higher anisotropy) and, consequently, less prone to size effects. For small fluences, the temperature dependence of H_E exhibits a nonmonotonic behavior, with a positive exchange bias[40] in a small temperature range. This is a known effect in Co/CoO systems and it is ascribed to the reversible switching of low anisotropy AFM grains.[41−43] Because this phenomenon is present only in the samples implanted at the lowest fluences, this indicates that the CoO formed in these samples is highly nanostructured and far from being stoichiometric, showing a low magnetic anisotropy (i.e., highly affected by scaling effects). Hence, this behavior can be correlated with the small amount of CoO in the grain boundaries inferred from the structural characterization. Interestingly, T_B for the high O fluences is substantially larger than for the bilayer ($T_B = 125$ K; see Figure 5b) or the one reported for Gaussian-like profile implantation ($T_B = 130$ K).[15] However, note that the obtained T_B for the bilayer system is rather low, indicating that the formed CoO by natural oxidation might be rather hyperstoichiometric and polycrystalline. In fact, FM/CoO bilayers with thick, highly monocrystalline and stoichiometric CoO show blocking temperatures close to the Néel temperature of bulk CoO.[44]

Figure 6 displays the training behavior of the bilayer and the sample implanted at 2×10^{17} ions/cm^2. The bilayer sample exhibits a very pronounced change between the first and second

dx.doi.org/10.1021/am400529r | ACS Appl. Mater. Interfaces 2013, 5, 4320−4327

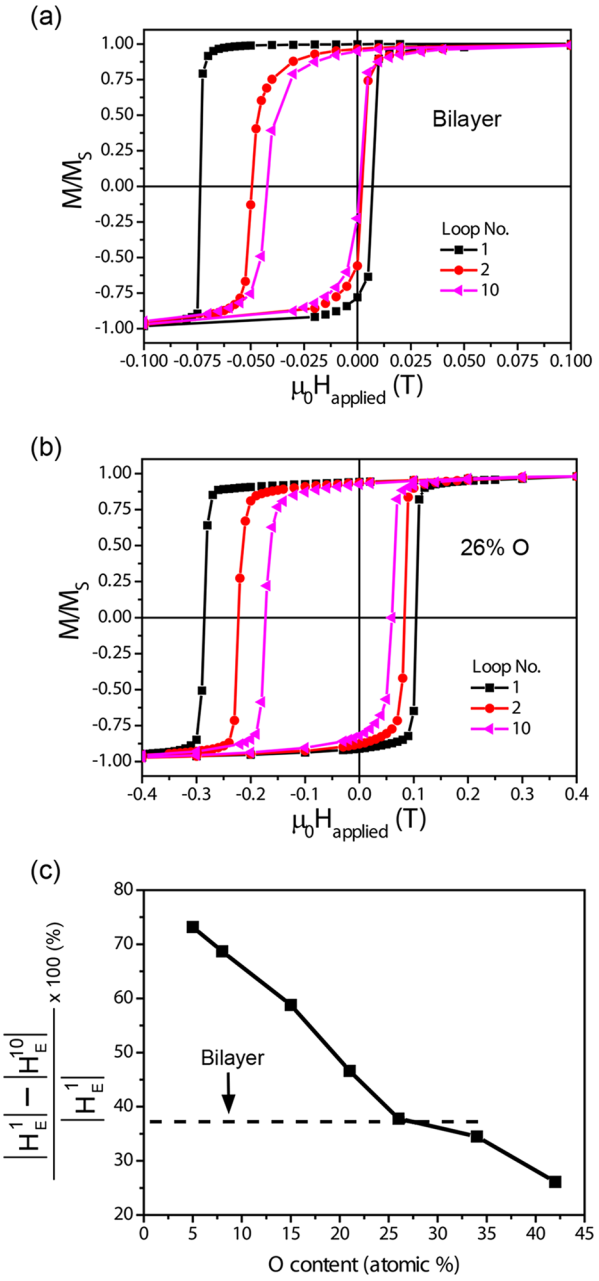

Figure 6. Consecutive SQUID loops at 10 K corresponding to (a) the bilayer and (b) the sample implanted at 2×10^{17} ions/cm^2 (26% O), respectively. (c) Dependence of the relative training, $((|H_E^1| - |H_E^{10}|)/|H_E^1|) \times 100$ (%), on the oxygen content for the different implanted samples. The relative training value for the bilayer is highlighted by a dashed line. The lines are connections between the data.

loop, typical for this type of samples.[21,45] On the other hand, the implanted samples show a more gradual change in H_E with cycling. A remarkable feature of the trained loops is that for the bilayer the trained loops display a considerable reduction in M_R, whereas loops of the implanted samples retain a rather unchanged M_R, which is considerably larger than that for the bilayers. For instance, although the bilayer shows bias corrected M_R/M_S (i.e., M_R/M_S at $H_{applied} = H_E$) values of 0.88 and 0.84 for the 2nd and 10th loops, the sample implanted at 2×10^{17} ions/cm^2 exhibits 0.92 and 0.89. Another important characteristic of the trained systems is the loss of exchange bias in the fully trained state. As can be seen in Figure 6c, the relative training $((|H_E^1| - |H_E^{10}|)/|H_E^1|) \times 100$ (%) is largest for the samples implanted with a low fluence, indicating that the spins in the less well-structured CoO (i.e., nanometric and non-stoichiometric) are more prone to reorientation by the applied field during cycling.[17,46] This behavior is to some extent analogous to that of CoO/Co systems with thin CoO layers.[47−49] Remarkably, for the largest fluences, the relative training becomes smaller than the one for the bilayers. Thus, for the optimum implanted samples, the loss in H_E in the fully trained state is smaller than for the bilayers. Notably, both the reduced relative training and the retained M_R in the fully trained loops of the implanted films are appealing parameters for perspective devices.

CONCLUSIONS

O ion implantation is confirmed as a successful technique to form AFM CoO in the interior of thin Co layers, giving rise to exchange bias. By properly selecting the implantation conditions and designing the thicknesses of the capping, Co and buffer layers, a rather uniform O profile across the Co layer thickness can be achieved using a single-energy ion implantation approach. This, contrary to both Co/CoO bilayers and Co films with a Gaussian-like O depth profile, results in superior EB properties, such as enhanced exchange bias strength, improved loop homogeneity, increased blocking temperature, decreased relative training or increased retained remanence in the trained state. This work proves the possibility to tailor the exchange bias properties by controlling the FM/AFM interface morphology via optimized ion implantation.

EXPERIMENTAL SECTION

Polycrystalline 30 nm thick Co thin films were grown by molecular beam epitaxy on thermally-oxidized Si (100) substrates which were previously covered with a 10 nm thick Au buffer layer. Subsequently, either a 15 nm or 30 nm thick Au capping layer was deposited in order to protect the Co from surface oxidation (i.e., from the formation of a CoO top layer which could result in EB). All layers were grown at room temperature at a pressure of approximately 3×10^{-10} mbar. Additionally, to serve as a reference, a film was grown in the same conditions but without capping layer, denoted as "bilayer" throughout the article, in order to deliberately form a top 2−3 nm CoO layer by exposing it to an O_2 atmosphere (5×10^{-4} mbar) for 5 min.

The calculation of the oxygen implantation profiles was carried out by using the TRIM (Transport of Ions in Matter) program, which is included in the SRIM (stopping range of ions in matter) package, after simulating the range and stopping of more than 1×10^4 ions along their track within the target material. The TRIM code is a Monte Carlo computer program, developed to determine principally the ion range and damage distribution in amorphous materials. TRIM uses several physical approximations to obtain high computer efficiency, while still maintaining accuracy. Two significant approximations are (i) using an analytic formula for determining atom−atom collisions, relying on a binary collision model, and (ii) evaluating only the stage of damage which is caused by the permanent displacement of lattice atoms from their original sites by the energy transfer received in nuclear collisions.[23,24] In order to run TRIM, the main input parameters are the species of projected ion, its energy and the density of the target material. Then, after averaging over a certain amount of ion histories, the distributions of different ion-related parameters, such as collision damage, can be obtained. Different conditions were simulated for various capping layer thicknesses, Co layer thicknesses, implantation energies and fluences and by introducing or not a buffer layer (see Figures 1 and 2 and Figure S1 in the Supporting Information).

On the basis of the TRIM simulations, the films with a Au (15 nm)/Co (30 nm)/Au (10 nm) (capping/FM/buffer) structure were then

dx.doi.org/10.1021/am400529r | ACS Appl. Mater. Interfaces 2013, 5, 4320−4327

implanted using O ions, with an energy of 40 keV, at fluences of 3×10^{16}, 5×10^{16}, 1×10^{17}, 1.5×10^{17}, and 2×10^{17} ions/cm^2. Basically, the implantation ions are obtained from ionization of a gas source of O_2 by means of electron bombardment which results in a oxygen rich plasma. The O ions are then extracted by applying a voltage. These ions are accelerated to the scheduled implantation energy by applying a voltage between the source and the rest of the beamline. Following, in order to only implant O, the ions are separated according to their mass by guiding them through a magnetic field. Finally, the ion beam is focused by means of a combination of electrostatic lenses and magnets in order to locally sweep the beam over the target material to achieve a homogeneous in-plane implantation. Moreover, aimed at producing larger amounts of CoO, samples with a Au (30 nm)/Co (30 nm)/Au (10 nm) structure were implanted at 3.5×10^{17} and 5×10^{17} ions/cm^2 using an energy of 50 keV. Note that thicker capping layers were grown in order to avoid its complete removal by the sputtering process inherent with the implantation process. Importantly, Rutherford backscattering spectrometry measurements (not shown) confirm the presence of a sufficiently thick remaining protective Au layer for all samples. According to TRIM, the O implantations result in an atomic O concentration at half depth of the Co layer of around 5, 8, 15, 21, 26, 34 and 42% for the films implanted at 3×10^{16}, 5×10^{16}, 1×10^{17}, 1.5×10^{17}, 2×10^{17}, 3.5×10^{17}, and 5×10^{17} ions/cm^2, respectively.

To structurally characterize the Co layer of the as-prepared film and its evolution with implantation fluence, ^{59}Co Nuclear Magnetic Resonance (NMR) experiments were carried out at low temperature (4.2 K), after zero-field-cooling from room temperature, using an automated and phase sensitive spin-echo spectrometer. The spectra were taken every 1 MHz in the frequency range 160−240 MHz at several values of the r.f. field amplitude. The Panissod protocol[50] is used to retrieve the value of the restoring field acting on electronic magnetization at a given frequency and to correct the NMR signal intensity accordingly.[51] Then, the resulting NMR spectra reflect the true number of nuclei resonating at a given frequency making it a very well-suited tool to study the structural and magnetic properties of Co-based alloys.[26,27,36]

The magnetic properties at room temperature were investigated by means of longitudinal magneto-optical Kerr effect (MOKE) measurements. To study the in-plane magnetic anisotropy, hysteresis loops were acquired at different angles between the sample orientation and the applied magnetic field. Longitudinal MOKE and superconducting quantum interference device (SQUID) magnetometry were used to study the exchange bias properties at 10 K. The samples were field cooled from room temperature to 10 K in an in-plane magnetic field of 400 mT. Training effects were studied at 10 K by performing consecutive hysteresis loops at 10 K. To estimate the blocking temperature (T_B), hysteresis loops were measured at different temperatures (starting from a fully trained state).

■ ASSOCIATED CONTENT

Supporting Information

Additional TRIM simulations. This material is available free of charge via the Internet at http://pubs.acs.org.

■ AUTHOR INFORMATION

Corresponding Author

*E-mail: Enric.MenendezDalmau@fys.kuleuven.be (E.M.); josep.nogues@uab.cat (J.N.); Kristiaan.Temst@fys.kuleuven.be (K.T.).

Notes

The authors declare no competing financial interest.

■ ACKNOWLEDGMENTS

This work was supported by the Fund for Scientific Research−Flanders (FWO), the Concerted Action of the KU Leuven (GOA/09/006 and GOA/14/007), the 2009-SGR-1292 project of the Generalitat de Catalunya, and the MAT2010-20616-C02 project of the Spanish Ministerio de Economía y Competitividad. The authors also acknowledge support by the EU FP 7 project SPIRIT (Support of Public and Industrial Research Using Ion Beam Technology, Contract No. 227012). E.M. thanks the Fund for Scientific Research−Flanders (FWO) for financial support.

■ REFERENCES

(1) Fassbender, J.; Ravelosona, D.; Samson, Y. *J. Phys. D: Appl. Phys.* **2004**, *37*, R179−R196.
(2) Chappert, C.; Bernas, H.; Ferre, J.; Kottler, V.; Jamet, J. P.; Chen, Y.; Cambril, E.; Devolder, T.; Rousseaux, F.; Mathet, V.; Launois, H. *Science* **1998**, *280*, 1919−1922.
(3) Menéndez, E.; Liedke, M. O.; Fassbender, J.; Gemming, T.; Weber, A.; Heyderman, L. J.; Suriñach, S.; Rao, K. V.; Deevi, S. C.; Baró, M. D.; Sort, J.; Nogués, J. *Small* **2009**, *5*, 229−234.
(4) Fassbender, J.; McCord, J. *J. Magn. Magn. Mater.* **2008**, *320*, 579−596.
(5) McGrouther, D.; Chapman, J. N.; Vanhelmont, F. W. M. *J. Appl. Phys.* **2004**, *95*, 7772−7778.
(6) Mougin, A.; Mewes, T.; Jung, M.; Engel, D.; Ehresmann, A.; Schmoranzer, H.; Fassbender, J.; Hillebrands, B. *Phys. Rev. B* **2001**, *63*, 060409(R).
(7) Demeter, J.; Meersschaut, J.; Almeida, F.; Brems, S.; Van Haesendonck, C.; Teichert, A.; Steitz, R.; Temst, K.; Vantomme, A. *Appl. Phys. Lett.* **2010**, *96*, 132503.
(8) Menéndez, E.; Martinavicius, A.; Liedke, M. O.; Abrasonis, G.; Fassbender, J.; Sommerlatte, J.; Nielsch, K.; Suriñach, S.; Baró, M. D.; Nogués, J.; Sort, J. *Acta Mater.* **2008**, *56*, 4570−4576.
(9) Marest, G.; Perez, A.; Gerard, P.; Mackowski, J. M. *Phys. Rev. B* **1986**, *34*, 4831−4839.
(10) Nogués, J.; Schuller, I. K. *J. Magn. Magn. Mater.* **1999**, *192*, 203−232.
(11) Nogués, J.; Sort, J.; Langlais, V.; Skumryev, V.; Suriñach, S.; Muñoz, J. S.; Baró, M. D. *Phys. Rep.* **2005**, *422*, 65−117.
(12) Dieny, B.; Speriosu, V. S.; Parkin, S. S. P.; Gurney, B. A.; Wilhoit, D. R.; Mauri, D. *Phys. Rev. B* **1991**, *43*, 1297−1300.
(13) Moser, A.; Takano, K.; Margulies, D. T.; Albrecht, M.; Sonobe, Y.; Ikeda, Y.; Sun, S. H.; Fullerton, E. E. *J. Phys. D: Appl. Phys.* **2002**, *35*, R157−R167.
(14) Gruyters, M.; Riegel, D. *J. Appl. Phys.* **2000**, *88*, 6610−6613.
(15) Demeter, J.; Menéndez, E.; Schrauwen, A.; Teichert, A.; Steitz, R.; Vandezande, S.; Wildes, A. R.; Vandervorst, W.; Temst, K.; Vantomme, A. *J. Phys. D: Appl. Phys.* **2012**, *45*, 405004.
(16) Demeter, J.; Menéndez, E.; Temst, K.; Vantomme, A. *J. Appl. Phys.* **2011**, *110*, 123902.
(17) Radu, F.; Zabel, H. *Springer Tracts Mod. Phys.* **2007**, *227*, 97−184.
(18) Radu, F.; Mishra, S. K.; Zizak, I.; Erko, A. I.; Dürr, H. A.; Eberhardt, W.; Nowak, G.; Buschhorn, S.; Zabel, H.; Zhernenkov, K.; Wolff, M.; Schmitz, D.; Schierle, E.; Dudzik, E.; Feyerherm, R. *Phys. Rev. B* **2009**, *79*, 184425.
(19) Tang, Y. J.; Smith, D. J.; Zink, B. L.; Hellman, F.; Berkowitz, A. E. *Phys. Rev. B* **2003**, *67*, 054408.
(20) van der Zaag, P. J.; Ijiri, Y.; Borchers, J. A.; Feiner, L. F.; Wolf, R. M.; Gaines, J. M.; Erwin, R. W.; Verheijen, M. A. *Phys. Rev. Lett.* **2000**, *84*, 6102−6105.
(21) Hoffmann, A. *Phys. Rev. Lett.* **2004**, *93*, 097203.
(22) Binek, Ch. *Phys. Rev. B* **2004**, *70*, 014421.
(23) Ziegler, J. F.; Biersack, J. P.; Littmark, U. In *The Stopping and Range of Ions in Solids*; Pergamon Press: New York, 1985; Vol. *1*, p 1.
(24) http://srim.org/. The TRIM (Transport of Ions in Matter) program is included in the SRIM (Stopping Range of Ions in Matter) package (SRIM-2011). Access date: 15/01/12.
(25) Nastasi, M.; Mayer, J. W.; Hirvonen, J. K. In *Ion−Solid Interactions: Fundamentals and Applications*; Cambridge University Press: Cambridge, U.K., 1996; p 4.

(26) Cerisier, M.; Attenborough, K.; Jedryka, E.; Wójcik, M.; Nadolski, S.; Van Haesendonck, C.; Celis, J. P. *J. Appl. Phys.* **2001**, *89*, 7083−7085.
(27) Jedryka, E.; Wójcik, M.; Nadolski, S.; Pattyn, H.; Verheyden, J.; Dekoster, J.; Vantomme, A. *J. Appl. Phys.* **2004**, *95*, 2770−2775.
(28) Chikazumi, S. In *Physics of Magnetism*; John Wiley & Sons: New York, 1978; p 254.
(29) Leighton, C.; Suhl, H.; Pechan, M.; Compton, R.; Nogués, J.; Schuller, I. K. *J. Appl. Phys.* **2002**, *92*, 1483−1488.
(30) Zha, C. L.; Dumas, R. K.; Fang, Y. Y.; Bonanni, V.; Nogués, J.; Akerman, J. *Appl. Phys. Lett.* **2010**, *97*, 182504.
(31) Lund, M. S.; Macedo, W. A. A.; Liu, K.; Nogués, J.; Schuller, I. K.; Leighton, C. *Phys. Rev. B* **2002**, *66*, 054422.
(32) Sort, J.; Nogués, J.; Suriñach, S.; Muñoz, J. S.; Baró, M.D.; Chappel, E.; Dupont, F.; Chouteau, G. *Appl. Phys. Lett.* **2001**, *79*, 1142−1144.
(33) Skumryev, V.; Stoyanov, S.; Zhang, Y.; Hadjipanayis, G.; Givord, D.; Nogués, J. *Nature* **2003**, *423*, 850−853.
(34) Menéndez, E.; Sort, J.; Langlais, V.; Zhilyaev, A.; Muñoz, J. S.; Suriñach, S.; Nogués, J.; Baró, J. M. *J. Alloys Compd.* **2007**, *434-435*, 505−508.
(35) Sort, J.; Dieny, B.; Nogués, J. *Phys. Rev. B* **2005**, *72*, 104412.
(36) Sort, J.; Suriñach, S.; Muñoz, J. S.; Baró, M. D.; Wojcik, M.; Jedryka, E.; Nadolski, S.; Sheludko, N.; Nogués, J. *Phys. Rev. B* **2003**, *68*, 014421.
(37) Nogués, J.; Skumryev, V.; Sort, J.; Stoyanov, S.; Givord, D. *Phys. Rev. Lett.* **2006**, *97*, 157203.
(38) Keller, J.; Miltényi, P.; Beschoten, B.; Güntherodt, G.; Nowak, U.; Usadel, K. D. *Phys. Rev. B* **2002**, *66*, 014431.
(39) Ghadimi, M. R.; Beschoten, B.; Güntherodt, G. *Appl. Phys. Lett.* **2005**, *87*, 261903.
(40) Nogués, J.; Lederman, D.; Moran, T. J.; Schuller, I. K. *Phys. Rev. Lett.* **1996**, *76*, 4624−4627.
(41) Prados, C.; Pina, E.; Hernando, A.; Montone, A. *J. Phys.: Condens. Matter* **2002**, *14*, 10063−10074.
(42) Demeter, J.; Teichert, A.; Kiefer, K.; Wallacher, D.; Ryll, H.; Menéndez, E.; Paramanik, D.; Steitz, R.; Van Haesendonck, C.; Vantomme, A.; Temst, K. *Rev. Sci. Instrum.* **2011**, *82*, 033902.
(43) Gredig, B. T.; Krivorotov, I. N.; Eames, P.; Dahlberg, E. D. *Appl. Phys. Lett.* **2002**, *81*, 1270−1272.
(44) Nowak, G.; Remhof, A.; Radu, F.; Nefedov, A.; Becker, H.-W.; Zabel, H. *Phys. Rev. B* **2007**, *75*, 174405.
(45) Brems, S.; Temst, K.; Van Haesendonck, C. *Phys. Rev. Lett.* **2007**, *99*, 067201.
(46) Ali, S. R.; Ghadimi, M. R.; Fecioru-Morariu, M.; Beschoten, B.; Güntherodt, G. *Phys. Rev. B* **2012**, *85*, 012404.
(47) Radu, F.; Etzkorn, M.; Siebrecht, R.; Schmitte, T.; Westerholt, K.; Zabel, H. *Phys. Rev. B* **2003**, *67*, 134409.
(48) Gredig, T.; Krivorotov, I. N.; Dan Dahlberg, E. *Phys. Rev. B* **2006**, *74*, 094431.
(49) Gredig, T.; Krivorotov, I. N.; Dan Dahlberg, E. *J. Appl. Phys.* **2002**, *91*, 7760−7762.
(50) Panissod, P.; Malinowska, M.; Jedryka, E.; Wójcik, M.; Nadolski, S.; Knobel, M.; Schmidt, J. E. *Phys. Rev. B* **2001**, *63*, 014408.
(51) The NMR restoring field can be regarded as an internal magnetic field which has to be overcome by an effective r.f. field in order to cause a rotation of the electronic magnetization inside a domain or a domain wall. This rotation in turn induces (via hyperfine interaction) oscillations of the local hyperfine field which are directly responsible for the nuclear Zeeman transitions (i.e., NMR). By monitoring the effective r.f. field required to maximize the NMR signal intensity at each resonance frequency, the corresponding restoring field dependence can be obtained. In principle, this frequency-dependent restoring field represents a variation of the magnetic stiffness in different parts of a sample. Any mechanism contributing to the local magnetic stiffness, such as magnetocrystalline anisotropy, exchange interaction or coercive field, will directly affect the value of the NMR restoring field and, consequently, the amplitude of the NMR signal. Therefore, in order to obtain the "true" NMR spectrum, where the signal intensity depends solely on the number of nuclei resonating at a given frequency, a correction for the experimentally determined local restoring field has to be applied.[40] Therefore, corrected NMR spectra reveal the distribution of hyperfine fields in the sample and, as these are very sensitive to the local atomic arrangement, insight on structural aspects, such as phases or defects, can be obtained.